Global Ocean Response to the 5-Day Rossby-Haurwitz Atmospheric Mode Seen by GRACE

Rui M. Ponte[1] and Michael Schindelegger[2]

[1]Atmospheric and Environmental Research, Inc., Lexington, MA, USA
[2]Institute of Geodesy and Geoinformation, University of Bonn, Bonn, Germany

Key Points:

- Daily GRACE data provide a first detailed look at the global ocean bottom pressure response to the 5-day Rossby-Haurwitz atmospheric mode
- GRACE data confirm the large-scale ocean dynamic response to barometric pressure and also reveal more spatially confined wind effects
- Derived flow fields are consistent with enhanced kinetic energy and dissipation rates over several topographic features in the Southern Ocean

Corresponding author: Rui M. Ponte, `rponte@aer.com`

Abstract

A dynamic response of the ocean to surface pressure loading by the well-known 5-day Rossby-Haurwitz mode in the atmosphere has been inferred from limited in situ tide gauge and bottom pressure data, but a global characterization of such response, including details at mid and high latitudes, has been lacking. Here we explore two daily data products from the Gravity Recovery and Climate Experiment (GRACE) mission to obtain a first quasi-global look at the associated ocean bottom pressure (p_b) signals at 5-day period. The previously reported in-phase behavior over the Atlantic basin, seesaw between the Atlantic and Pacific, and westward propagation in the Pacific are all seen in the GRACE solutions. Other previously unknown features include relatively strong responses in the Southern Ocean and also some shallow coastal regions (e.g., North Sea, East Siberian shelf, Patagonian shelf). Correlation analysis points to the Rossby-Haurwitz surface pressure wave as the main forcing for the observed large-scale p_b anomalies, while wind-driven signals are more spatially confined. The GRACE observations are found to be consistent with in situ p_b data and also with model simulations of the 5-day ocean variability where no in situ data is available. Inferences on energetics based on data and model results point to decay time scales shorter than the oscillation period, with substantial kinetic energy and dissipation located over a few topographic features in the Southern Ocean. Results illustrate the potential of space gravity measurements for examining large-scale oceanic variability at sub-weekly periods.

Plain Language Summary

A dynamic response of the ocean to surface pressure loading by a well-known 5-day mode in the atmosphere has been inferred from limited in situ data, but a global characterization of such response has been lacking. Here we explore two daily data products from the Gravity Recovery and Climate Experiment (GRACE) mission to obtain a first near-global look at the associated ocean bottom pressure (p_b) signals near 5-day period. Previously observed spatially homogeneous behavior over the Atlantic basin, seesaw between the Atlantic and Pacific, and westward propagation in the Pacific are all seen in the GRACE solutions. Other previously unknown features include enhanced responses in the Southern Ocean and also some shallow coastal regions (e.g., North Sea, East Siberian shelf, Patagonian shelf). Surface atmospheric pressure is the main forcing for the observed large-scale p_b anomalies, while wind-driven signals are more spatially confined. The GRACE observations are consistent with in situ p_b data and also with model simulations. The oscillation is strongly damped on time scales shorter than its period, with substantial currents and frictional dissipation located over a few topographic features in the Southern Ocean. Results illustrate the potential of GRACE measurements for examining large-scale oceanic variability at sub-weekly periods.

1 Introduction

Global scale interbasin mass exchange is well known to result from the barotropic ocean response to lunar-solar tidal forcing, which involves complex wave and resonant dynamics at diurnal and semi-diurnal periods. Although not as well studied as the tides, a similar behavior can be elicited by non-tidal atmospheric forcing at rapid (sub-weekly) time scales. In particular, surface atmospheric pressure (P_a) variations have been found to drive a global scale dynamic response involving interbasin mass exchange, in both non-resonant regimes (Ponte, 1997) and near-resonant regimes through the excitation of global normal modes (Ponte & Hirose, 2004; Kusahara & Ohshima, 2014). Surface winds are also a relevant forcing mechanism in this context but at longer (monthly) time scales (Stepanov & Hughes, 2006).

Knowledge of such non-tidal, atmospherically forced mass signals is important in several ways. Given the rapid time scales and large spatial scales involved, they can be a source of aliasing for space geodetic missions like the Gravity Recovery and Climate Experiment (GRACE, Flechtner et al., 2016) and can also affect other geodetic parameters like Earth rotation and crustal loading (e.g., van Dam et al., 2012; Harker et al., 2021). In an oceanographic context, they can involve significant volume transports (Bryden et al., 2009) and be the source of misinterpretation when inferring the circulation from bottom pressure data (Bingham & Hughes, 2008). More generally, interbasin mass exchange can critically depend on domain geometry, topography and dissipation, among other factors, and its study can ultimately reveal important details about barotropic ocean dynamics. Lack of adequate global observations, however, has hindered progress in understanding, modeling and estimating such signals (e.g., Ponte & Hirose, 2004; Park & Watts, 2006)

For interbasin mass exchange, observations of sea level and bottom pressure (p_b) are most relevant. Satellite altimeters provide near-global coverage but repeat sampling rates are nominally 10 days or longer. In addition, sea level can contain baroclinic signals not related to mass, which is more directly inferred from p_b observations. Although a number of in situ p_b records exist, these are very sparse in space and time and can reflect short scale local signals not relevant to our problem. Satellite gravimetry has provided global p_b data products with nominal temporal resolution of one month (Tapley et al., 2019; Landerer et al., 2020), but recent work involving comparisons with altimeter and in situ p_b data, as well as with various ocean models, has indicated the potential to estimate p_b from space down to periods ~ 4 days (Bonin & Save, 2020; Schindelegger et al., 2021).

Well-known, basin-scale mass variability occurs in the dynamic response to the $\sim$5-day Rossby-Haurwitz wave in surface atmospheric pressure P_a (R. Madden & Julian, 1972; R. A. Madden, 2019). Tropical tide gauge analyses revealed the Pacific-wide nature of the signal (Luther, 1982) and its presence in the tropical South Atlantic (Woodworth et al., 1995). Observing the signal in extra-tropical latitudes remained difficult because of higher synoptic atmospheric "noise" (Mathers & Woodworth, 2004), but its Atlantic-wide nature extending to 37°N was described by Park and Watts (2006), and basin-scale averages of altimeter data were able to reveal the interbasin nature of the signal (Hirose et al., 2001). Thomson and Fine (2021) have confirmed earlier findings using analyses of bottom pressure data from the DART (Deep-ocean Assessment and Reporting of Tsunamis) network, but a data-constrained description on global scales, including details of the structure at mid and high latitudes, has remained elusive.

In this work, we explore two high-sampling satellite gravimetry products (Kvas et al., 2019; Bonin & Save, 2020) to examine p_b variability over the global oceans at $\sim$5-day period. Results confirm the importance of the global dynamic response to P_a, highlight new spatial features of the $\sim$5-day signal, point to strong dissipation rates likely associated with strongest flows over topographic features, and illustrate the usefulness of satellite gravimetry data for the study of basin-scale p_b fluctuations at subweekly periods. All data and models are described in section 2. The structure of the observed 5-day p_b variability is presented in Section 3 and assessed against other data in Section 4. Relation of p_b anomalies to atmospheric forcing is treated in Section 5, and energetics and dissipation issues are discussed in Section 6. A summary of findings and final considerations are provided in Section 7.

2 Observations, Models, and Basic Methods

We use the same 3-year (2007–2009) daily GRACE datasets as in Schindelegger et al. (2021). These gravity field series come from CSR (Center for Space Research at University of Texas, Austin, Bonin & Save, 2020) and ITSG (Institute of Geodesy at Graz University of Technology, release ITSG-Grace2018, Mayer-Gürr et al., 2018; Kvas et al., 2019). Each solution draws on some form of regularization, as the GRACE ground track coverage within 24 hours is insufficient to resolve globally distributed mass changes into wavelengths of $\mathcal{O}(1000 \text{ km})$. Because geophysical processes are not random, a common approach to regularization is to constrain the gravity field's expected evolution in time. The CSR method derives constraints from accumulated monthly GRACE signals and performs the inversion on a per-grid-point ("mascon") basis every time the satellites are within 250 km from a particular mascon (2–4 days in mid-latitudes, Bonin & Save, 2020). By contrast, the ITSG series are furnished by a recursive Kalman filter operating on spherical harmonics up to degree and order $n = 40$. Each ITSG daily solution is stabilized with information from nearby days, as conveyed by numerical model-based process dynamics (i.e., temporal correlations) in the Kalman filter's stochastic component (Kurtenbach et al., 2012).

For both CSR and ITSG, recovery of geophysical signals is relative to the Atmosphere and Ocean De-Aliasing Level-1B (AOD1B) product (releases RL05 or RL06, Dobslaw et al., 2017a). The ocean model underlying AOD1B, which we also analyze for ∼5-day signals below, is a 1° baroclinic forward simulation forced by atmospheric pressure, wind stress, and buoyancy fluxes. In synthesizing the daily GRACE fields into p_b variations on a regular 1° grid, we have restored the respective AOD1B coefficients for the ocean (the GAD product, Dobslaw et al., 2017b), including degree $n = 1$ terms. Note that the ITSG fields are global, while the CSR mascon grids available to us do not extend to latitudes beyond ±66°. All additional processing steps applied to these data (1000-km smoothing and gap filling of CSR, adoption of a coastal buffer) are as in Schindelegger et al. (2021). The latter study also introduces in-situ p_b series from 40 bottom pressure recorders (BPRs, Gebler, 2013), which we use here to validate the 5-day band variability in the two GRACE products. Measurements from 2007 to 2009 at each site (sometimes from successive deployments) were drift-corrected, tidally analyzed, and averaged into daily values. The shortest records have 182 days of observations.

To interpret satellite-based p_b variability with ∼5-day periodicity in terms of relevant forcing (loading by P_a, wind stress), we perform a small number of forward simulations with a barotropic (2D) time-stepping model referred to as DEBOT (David Einšpigel's Barotropic Ocean Tide model, Einšpigel & Martinec, 2017). The model uses a near-global ⅓° latitude-longitude grid, and its p_b diagnostics are known to compare favorably with GRACE, particularly on sub-weekly time scales (Schindelegger et al., 2021). Energy losses are conveyed by two stress terms $\mathcal{F}_b + \mathcal{F}_w$ (in units of m^2 s^{-2}), related to quadratic bed friction (subscript b) and the conversion of barotropic energy to baroclinic waves (w) at gradients of topography (Carrère & Lyard, 2003)

$$\mathcal{F}_b + \mathcal{F}_w = C_d\mathbf{u}|\mathbf{u}| + L\overline{N}(\nabla H)^2\mathbf{u} \tag{1}$$

Here, $C_d = 0.0025$ is a non-dimensional bottom drag coefficient, $\mathbf{u}$ is the depth-averaged velocity vector, $L = 5.0\ 10^4$ m represents a tunable length scale estimate, $\overline{N}$ is the vertically averaged buoyancy frequency, and H denotes water depth. For simplicity, we switch off the model's time step-wise handling of self-attraction and loading effects (Stepanov & Hughes, 2004). All forcing fields are derived from ECMWF (European Centre for Medium-Range Weather Forecasts) Interim Reanalysis (ERA-Interim, Dee et al., 2011).

Hereinafter, we extract the ∼5-day signal in various datasets (GRACE, P_a, DEBOT dynamic residuals) using a 5$^{\text{th}}$-order Butterworth band-pass filter with cut-off frequencies placed at 0.175 and 0.233 cpd (cycles per day) corresponding to periods of 5.7 and 4.3 days, respectively. These frequencies are commensurate with choices in Thomson and Fine (2021) and aligned with half-power points of the zonal wavenumber $k = -1$ Rossby-Haurwitz mode in global air pressure spectra (Sakazaki & Hamilton, 2020, their Figure 11). To examine the space-time structure of coherent p_b variability in this frequency band, we apply complex-valued empirical orthogonal function (CEOF) analysis (e.g., Barnett, 1983; Bouzinac et al., 1998) to the analytical signal

$$p_b\,(\mathbf{x}, t) + ip_b^*\,(\mathbf{x}, t) \tag{2}$$

Here, t is time, $i \equiv \sqrt{-1}$, and $p_b^*\,(t)$ is the Hilbert transform of the time series at a particular location $\mathbf{x}$. The eigenvectors (CEOFs or spatial modes) of the covariance matrix and their associated principal components (temporal modes) are both complex and therefore readily separated into amplitude and phase functions. We compute spatial phases as in Barnett

(1983) but introduce the imaginary part with negative sign so that propagation is in the direction of increasing phase. Throughout the paper, we express magnitudes of a particular CEOF mode as standard deviation (occasionally still referred to as "amplitude"), obtained from calculating the variance of the mode after reconstructing the respective time series at location $\mathbf{x}$. For comparison with amplitude charts in the literature (e.g., Ponte, 1997; Thomson & Fine, 2021), our maps should be multiplied with $\sqrt{2}$. Units of p_b are SI (Pa) in equations but quantified as equivalent water height in the text and figures.

3 Global Structure of the Observed 5-Day Signal

Figure 1 displays the global spatial structure of the ∼5-day dynamic variability, computed from the CEOF decomposition of the daily GRACE series. For both data products, the leading CEOF (abbreviated as CEOF1) of 25 computed eigenvectors explains roughly a quarter of the total variance in the 5-day band, dropping to ∼18% when the spectral filtering (Section 2) is extended to periods from 2 to 7 days. The mode reveals an amplitude structure of weak maxima (∼4–5 mm) in the middle of the North Pacific, South Indian and South Atlantic, and larger values (>6 mm) in a few areas in the Southern Ocean and some shallow coastal regions (e.g., North Sea, Patagonian Shelf). The high latitudes depicted by the ITSG product show a tendency for decreasing amplitudes towards the Antarctic coast and values in the Arctic <3 mm. There is considerable temporal modulation of the CEOF amplitude (not shown) on monthly timescales but without a discernible seasonal dependence.

The phases of the CEOF1 for CSR and ITSG (Figure 1e,f) are also very similar on the large scale, apart from differences in some shorter scale features in regions of minimum amplitude (e.g., northeastern North Pacific), which can represent amphidromic points. The Atlantic shows fairly homogeneous values around 30–60°. In the Pacific, phases are more variable but for the most part around $180° \pm 30°$, and thus roughly out of phase with the Atlantic. In addition, there is an indication of westward propagation at latitudes ∼20°–40°, particularly in the Pacific basin interior away from the coasts. Westward propagation seems to extend to the Southern Ocean sector of the Indian Ocean, between Australia and Antarctica. Otherwise, for the Indian Ocean most phase values are between −75° and −15°. In any case, phase differences suggest long spatial scales compared to the basins.

The second CEOF (CEOF2, Figure 2), which accounts for an additional ∼14% of the total variance for CSR (12% for ITSG), shows a somewhat different behavior, but still largely consistent for the two products. The dominant feature is the enhanced standard deviation (>5 mm) over a large part of the Pacific sector of the Southern Ocean, surrounding a minimum at about 120°W. Other places of relatively higher variability occur in the Arctic (for ITSG in Figure 2b), particularly over the East Siberian shelf, the Gulf of Alaska, Hudson Bay, and the shallow North Sea and Patagonian shelf.

The phase structure for CEOF2 exhibits clear westward propagation across the whole Pacific basin, and indicates spatial scales much shorter than those associated with CEOF1 (cf. Figure 1). There is also a clear amphidromic point centered at around 120°W, 50°S, with signals propagating counterclockwise. Phases in the deep Arctic are fairly homogeneous but eastward propagation is seen along the East Siberian shelf, coincident with maximum amplitudes.

4 Assessing GRACE-based Estimates

As evident from Figures 1 and 2, the assimilation of GRACE data modifies the background model and brings the ITSG fields closer to those of CSR. This provides a useful measure of the quality of both products and underscores the value of the GRACE data in the Kalman filter solution. However, ITSG and CSR results include common degree-1 contributions that are purely determined from the AOD1B output. For comparison, Figures 1d,h show the CEOF1 of the AOD1B degree-1, with typical standard deviations of a few mm, maxima near the equator, and a large scale phase pattern resembling that in the ITSG and CSR CEOF1 (Figures 1e,f). Nevertheless, much of the detail in amplitude and phase of the latter is associated with the higher degrees and how they are modified by the information extracted from the GRACE data. In particular, comparisons of the ITSG product and the AOD1B model used in the respective Kalman filter solution reveal visible differences in amplitude and phase of CEOF1 in the Pacific sector of the Southern Ocean (Figures 1b,c,f,g). Similar changes can be seen for CEOF2 (Figures 2b,c,e,f), regarding for example the phase propagation in the Pacific basin.

Aside from their similarities, the characteristics of the variability associated with both estimated CEOFs are qualitatively consistent with previous analyses of in situ and altimeter measurements, including the approximate in-phase behavior in the Atlantic (Woodworth et al., 1995; Mathers & Woodworth, 2004; Park & Watts, 2006) and out-of-phase behavior between the Atlantic and Pacific (Hirose et al., 2001), and the westward phase propagation in the Pacific (Luther, 1982). For a more quantitative assessment of the GRACE-based estimates of the 5-day signal, we turn to comparisons with the 40 BPR time series in Figure 3. Both the full variability in the 5-day band and that synthesized in CEOF1 and CEOF2 (Figures 1 and 2) are considered. Although the BPRs are located mostly outside regions of peak 5-day variability observed by GRACE (Figure 3a), they provide broad enough coverage of the Pacific and Atlantic basins where the large scale behavior of the 5-day response is clear (Figures 1 and 2).

Based on the full p_b variability in the 5-day band (Figure 3a), the root-mean-square (RMS) differences of the GRACE and BPR observations (median values of 0.22 and 0.29 cm for ITSG and CSR, respectively) are considerably lower than the BPR RMS values (median of 0.45 cm; Figure 3b,c). The BPR variance explained by ITSG hovers mostly around 60 to 90% (median value of 77%; Figure 3d), while values for CSR are lower (median value of 58%; Figure 3e), consistent with the generally higher noise levels in CSR fields found by Schindelegger et al. (2021).

For comparison, results based on equivalent AOD1B series (not shown) yield a median RMS difference of 0.23 cm and variance explained of 71%, which confirms the value of GRACE data in improving the quality of the ITSG p_b estimates. The AOD1B comparisons with the BPR data are, however, substantially better than those for CSR, suggesting sensitivity of the GRACE-based fields to the gravity field retrieval procedure and, presumably, to the quality of the de-aliasing model (AOD1B RL05 or RL06).

If one compares results from the modal decomposition to the BPRs (Figures 3b–e), the variance explained by CEOFs is comparatively smaller than when using the full variability, as expected. The RMS differences and variance explained values for ITSG and CSR are, however, more similar than when using the full variability. Results suggest that the CEOFs filter out some of the higher noise in the CSR series, which is probably to a large extent spatially uncorrelated on basin scales.

Aside from noise in both GRACE and BPR data, one should expect differences in their behavior because while GRACE provides averaged values on scales $\sim$300 km, BPRs provide point measurements that can sense shorter scales. An independent, alternative assessment of the GRACE fields on the largest scales can be obtained by examining Earth rotation data. Using data sets and methods described in detail by Harker et al. (2021), we have used the GRACE-derived p_b fields to calculate the implied excitation of polar motion and compared results with geodetic observations of the same quantity that were corrected for atmospheric effects. The GRACE-derived excitations due to changes in the oceanic mass distribution, either using the full variability in the 5-day band or the CEOFs as a basis, can explain substantial portions of the observed geodetic minus atmospheric residual variance in polar motion excitation (up to 46% for one coordinate direction). These analyses, together with results in Figure 3, confirm the realism of the GRACE-based estimates of p_b variability in the 5-day band.

5 Relation to Forcing

Previous data and model analyses have clearly associated the observed 5-day variability in tide gauge and BPRs to P_a forcing (e.g., Luther, 1982; Ponte, 1997; Mathers & Woodworth, 2004; Park & Watts, 2006; Thomson & Fine, 2021). Here, we explore the relation between the temporal modes of p_b CEOFs from ITSG (Figures 1 and 2) and ERA-Interim P_a by calculating lagged regressions (at 0, ± 1, and ± 2 days) between real-valued time series of both quantities (Figure 4). To mitigate the impact of synoptic scale variability, particularly strong over extratropical latitudes, the band-pass filtered P_a fields were restricted to long zonal wavelengths by convolving them with a Tukey window of half-length 8, with a center point at wavenumber $k = 0$.

For the case of CEOF1 (Figures 4a–e), there is a zonal wavenumber one, westward propagating pattern, which is clear over most latitudes, with a tendency for enhanced values over mid latitudes and weakening toward the tropics. These features are revealing of the Rossby-Haurwitz wave originally identified by R. Madden and Julian (1972). The CEOF1 in Figure 1 is, thus, strongly linked to the 5-day Rossby-Haurwitz P_a variability, which is consistent with earlier findings based on tide gauge and BPR analyses (Luther, 1982; Mathers & Woodworth, 2004; Park & Watts, 2006; Thomson & Fine, 2021).

A westward propagating, zonal wavenumber one structure is also apparent for CEOF2 case over tropical latitudes but, despite the large-scale coherent pattern, the results are not formally significant at the 95% confidence level (Figures 4f–j). Significant values at higher latitudes tend to occur in smaller scale patches, associated with dipoles or higher wavenumbers. These regions (e.g., Arctic Ocean, Gulf of Alaska, Bellingshausen Basin) approximately coincide with enhanced CEOF2 amplitudes in Figure 2 and point to more localized forcing effects. In this regard, there is a hint of eastward propagation in the Bellingshausen Basin, which suggests influence of synoptic systems, possibly involving also related wind forcing.

The roles of barometric pressure and wind stress can be further elucidated by comparing DEBOT experiments with 6-hourly broadband P_a and wind forcing with one that only includes loading by P_a (years 2007–2009). The amplitudes and phases of CEOF1 extracted from the simulation with combined P_a and wind forcing (Figure 5a,c) closely resemble those of CEOF1 in Figure 1, testifying to the ability of DEBOT to reproduce the 5-day signal in the GRACE-based fields. In the P_a-only experiment (Figure 5b,d), the enhanced amplitudes in the Southern Ocean, particularly in its Pacific sector, as well as in shallow coastal regions (e.g., Patagonian shelf, North Sea), are considerably reduced, and relatively short scale phase patterns, including the eastward and westward phase propagation near the Bellingshausen Basin, are mostly absent. These features are thus likely to be substantially associated with wind driving, while the basin-scale patterns are mostly related to pressure loading. In particular, integrating the model for 60 days with the 5-day P_a harmonic deduced from the lagged regression analysis (Figure 4) leads to amplitude and phase patterns very close to the one obtained with the full P_a forcing (Figure 5b,d). Together, these results confirm the importance of the barometric pressure variability associated with the Rossby-Haurwitz mode to the large-scale dynamic ocean response near 5-day periods.

6 Frictional Decay and Energetics

Questions as to how, where, and at what rates the oceanic 5-day oscillation expends its energy through frictional processes remain far from fully solved. In general, analyses of both sea level and p_b records, often used in conjunction with ocean models, favor a highly damped oceanic response with a typical energy e-folding decay scale, t_e, of about 3 days (Luther, 1982; Ponte, 1997). However, the available potential energy (PE) decay rate constrained by these types of data appears almost insensitive to the amount of damping in the 5-day band, as evident from dedicated numerical simulations (Thomson & Fine, 2021). Greater variability with assumed frictional drag coefficients is seen for t_e of kinetic energy (KE), a term that exceeds PE in magnitude by a factor of $\gtrsim 2$ (see again Thomson & Fine, 2021).

In this light, it is helpful to consider global integrals of important energy balance terms from the results presented thus far. In particular, using CEOF1 (ITSG) maps of bottom pressure and regressed P_a patterns, shown in Figures 1 and 4, one can estimate PE and the rate of work done by the atmosphere on the ocean (Ponte, 2009). Time averages for these quantities, computed over a 5-day cycle, are $\sim 14 \cdot 10^{12}$ J and 131 MW, respectively. Adopting ratios of PE/KE from DEBOT solutions (2.15 in the run with harmonic P_a forcing), we obtain an estimate of $\sim 44 \cdot 10^{12}$ J for the mean total energy. Dividing this value by the work rate gives an approximate energy replenishment or equivalently a depletion time scale of ~ 3.9 days, considerably shorter than the period of the oscillation. Despite the approximate nature of our calculations, these values are consistent with the large dissipation rates alluded to above.

To solidify existing values for decay time scales (linear or exponential) and explore possible mechanisms and locations of the underlying dissipation, empirical knowledge of currents, and thus KE, would be desirable. Here we report on a regional and largely experimental mapping of horizontal kinetic energy fields, KE($\mathbf{x}$), from 5-day p_b charts in the Southern Ocean, based on recipes laid out for strictly harmonic signals (i.e., gravitational tides, Ray, 2001; Madzak et al., 2016). Writing amplitudes (A) and phases (ϕ) of CEOF1 as $\hat{p}_b = Ae^{-i\phi}$ with time dependence $e^{i\omega t}$ ($\omega = 0.2$ cpd), one can estimate volume transports $(U, V) = H\mathbf{u}$ by fitting the depth-averaged, linearized equations of motion in a least squares sense

$$i\omega\hat{U} - f\hat{V} + \frac{\kappa\hat{U}}{H} = -\frac{H}{\rho_0 a\cos\varphi}\frac{\partial\hat{p}_b}{\partial\lambda} \tag{3}$$

$$i\omega\hat{V} + f\hat{U} + \frac{\kappa\hat{V}}{H} = -\frac{H}{\rho_0 a}\frac{\partial\hat{p}_b}{\partial\varphi} \tag{4}$$

$$\frac{1}{a\cos\varphi}\left[\frac{\partial\hat{U}}{\partial\lambda} + \frac{\partial(\hat{V}\cos\varphi)}{\partial\varphi}\right] = \frac{-i\omega}{\rho_0 g}\left[\hat{p}_b - \hat{P}_a\right], \tag{5}$$

Here, (φ, λ) represent latitude and longitude on a sphere of radius a, ρ_0 is mean seawater density, and the Coriolis parameter f is oriented to the local vertical. Provided that the continuity constraint (Eq. 5) is strongly enforced (i.e., weighted) relative to Eqs. (3) and (4), the least squares fit only weakly depends on the prior assumption about dissipation (Egbert & Ray, 2001; Ray, 2001). The linear drag coefficient κ in our implementation takes a value of 0.005 m s^{-1}, but nearly identical results in the inversion were obtained with $\kappa \in (0.0001, 0.02)$ m s^{-1}.

Upon substituting gridded fields for $\hat{p}_b$ and $\hat{P}_a$ (from regression, Figure 4), we solve the overdetermined system (Eqs. 3–5) using direct matrix inversion in a rectangular domain spanning much of the Southern Ocean ($-70° \leq \varphi \leq -30°$, $130° \leq \lambda \leq 355°$). Local energetics, evaluated inline in DEBOT integrations, suggest that $\sim$45% of the 5-day signal's KE and global dissipation rate ($\sim$60 MW of the quoted 131 MW pressure work) reside in this area. For simplicity, we use a finite-difference B-grid (Arakawa & Lamb, 1977) with 1° spacing for the least-squares fit, omit effects of self-attraction and loading, and forgo specification of no-flow boundary conditions. Considering these refinements or extending the inversion to global scales would call for more involved numerics and was deemed infeasible within the study at hand.

Figure 6 presents maps of KE($\mathbf{x}$) deduced from fitting dynamics and CEOF1 from either AOD1B or ITSG, along with time-mean values of KE($\mathbf{x}$) calculated during time-stepping DEBOT with harmonic P_a forcing. The three solutions have several features in common and generally locate areas of enhanced KE($\mathbf{x}$), and therefore horizontal currents, over distinct bathymetric elements such as the Macquarie Triple Junction (61°S, 160°E), the Pacific Antarctic Ridge, the southern tip of the East Pacific Rise (52°S, 120°W), and the Mid-Atlantic Ridge near 40°S. Less agreement is seen around Patagonia, where the inversion results are affected by wind-driven signals in p_b (cf. Figure 5), inhibiting also the detection of the intensified flow (KE($\mathbf{x}$) ~ 7 J m^{-2} in DEBOT) across the Malvinas–Falkland Escarpment at depths between 1000 and 3000 m.

Additional contributions from wind forcing (e.g., over the East Pacific Rise) cannot be ruled out, but there is clear evidence that their impact on the gradient computation (Eqs. 3–4) is far less pronounced with the ITSG GRACE fields than with AOD1B, providing for a better match with DEBOT diagnostics and a cleaner view of the energetics in the 5-day band. In quantitative terms, we find an area-integrated KE value in the focus region of $\sim 13{\cdot}10^{12}$ J from ITSG, similar to what is inferred directly from DEBOT ($\sim 11{\cdot}10^{12}$ J). We caution, though, against taking the GRACE-based area integral at face value, especially given the low spatial resolution of the inversion and the entanglement of pressure- and wind-driven signals in the utilized p_b maps. The agreement is nevertheless encouraging and lends credence to the global KE value of $23{\cdot}10^{12}$ J assumed in our inference of the oscillation's energy depletion time scale of 3.9 days.

7 Conclusions and Final Considerations

We have exploited the existence of daily GRACE-based p_b observations to revisit the nature of the global ocean response to the $\sim$5-day Rossby-Haurwitz atmospheric mode. Our CEOF analysis of GRACE-derived fields is consistent with a basin-scale dynamic response to P_a associated with the Rossby-Haurwitz mode, as inferred from previous in situ data and model analyses (Luther, 1982; Woodworth et al., 1995; Mathers & Woodworth, 2004; Ponte, 1997; Park & Watts, 2006; Thomson & Fine, 2021). In addition, finer scale structures in the Southern Ocean and over shallow regions (e.g., North Sea, Patagonian shelf) are also seen in the GRACE data, and barotropic model simulations indicate that they are mostly related to wind forcing rather than P_a.

Contributions of wind forcing to the shorter scale features of the CEOFs in the Southern Ocean and in shallow regions are somewhat puzzling, as winds associated with the large-scale Rossby-Haurwitz mode should be very weak, and there is no prior evidence of large-scale coherence between p_b and winds near 5-day period (e.g., Park & Watts, 2006; Zhao et al., 2017). There is nevertheless considerable energy in synoptic weather systems near 5 days, with associated surface winds capable of generating strong p_b variability, particularly over shallow regions. Our CEOF analysis and DEBOT results suggest that some of this locally driven p_b variability can be coherent with the large-scale P_a-driven bottom pressure signals associated with the Rossby-Haurwitz mode. This is turn points to possible coherent variability between the latter and local synoptic systems. In this regard, synoptic systems have been advanced as possible excitation mechanisms for the Rossby-Haurwitz mode, which in turn can also modulate the synoptic variability (King et al., 2015). Whether localized synoptic variability can be related to the Rossby-Haurwitz mode, thus affecting the structure of the ocean response at 5-days as suggested by our results, is a hypothesis worth further exploration in future efforts.

The availability of global data sets such as those provided by the daily GRACE inversions allows for a number of analyses not otherwise possible with sparse in situ observations. Examples are the determination of the relation between the Rossby-Haurwitz P_a loading and the global ocean 5-day variability in Section 5 and the related estimates of local and global energetics in Section 6. In particular, global p_b fields allow one to invert for the flow field and obtain estimates of local kinetic energy (Section 6). Combining estimates of local energy flux divergence (Egbert & Ray, 2001) and of work done by the atmosphere can yield useful information on local dissipation rates. Preliminary calculations of this kind point to enhanced dissipation over several topographic features of the Southern Ocean, most prominently the Pacific Antarctic Ridge and the Malvinas–Falkland Escarpment, as might be anticipated from Figure 6. This insight lends support to the use in models of wave drag parameterizations representing effects of rough topography, such as those included in DEBOT (see Eq. 1).

More generally, these and related analyses can be an important part of broader efforts to test ocean models at high frequencies (cf. Schindelegger et al., 2021). In this regard, differences between ITSG and AOD1B solutions (Figures 1 and 2) point to potential issues with how AOD1B deals with representation of dissipation and/or topographic influences on the 5-day variability in the Southern Ocean. Future AOD1B releases, currently under preparation, will likely incorporate improvements to deal with these and other issues revealed by comparisons with observations. Our findings indicate that GRACE data sampled at higher than nominal monthly rates contain potentially useful information at periods as short as 5 days, which should be used to constrain and improve ocean models. Eventually, dynamical models run with data assimilation, including GRACE observations, should be employed to derive optimal estimates of sub-monthly p_b signals, as well as to improve model representation of sub-grid scale processes.

Acknowledgments

Work at AER was supported by NASA and the GRACE Follow-On Science Team through grant 80NSSC20K0728. MS acknowledges funding by the Austrian Science Fund (FWF, grant P30097-N29) and the German Research Foundation (DFG, grant SCHI 1496/4-1).

The datasets used in this study are available from the following links: ITSG-Grace2018 (`ifg.tugraz.at/ITSG-Grace2018`), CSR swath (`https://doi.org/10.18738/T8/95ITIK`), ADO1B releases (`ftp://isdcftp.gfz-potsdam.de/grace/Level-1B/GFZ/AOD/`), and ERA-Interim (`https://apps.ecmwf.int/datasets/data/interim-full-daily/`). Codes to process the daily ITSG-Grace2018 solutions and replicate both the CEOF analysis and the least-squares inversion for this dataset have been placed on `https://doi.org/10.5281/zenodo.5744953`.

References

Arakawa, A., & Lamb, V. R. (1977). Computational design of the basic dynamical processes of the UCLA general circulation model. *Methods in Computational Physics: Advances in Research and Applications*, *17*, 173–265.

Barnett, T. P. (1983). Interaction of the Monsoon and Pacific trade wind system at interannual time scales part I: The equatorial zone. *Monthly Weather Review*, *111*, 756–773.

Bingham, R. J., & Hughes, C. W. (2008). Determining North Atlantic meridional transport variability from pressure on the western boundary: A model investigation. *Journal of Geophysical Research: Oceans*, *113*(C9). doi: https://doi.org/10.1029/2007JC004679

Bonin, J. A., & Save, H. (2020). Evaluation of sub-monthly oceanographic signal in GRACE "daily" swath series using altimetry. *Ocean Science*, *16*(2), 423–434. Retrieved from `https://os.copernicus.org/articles/16/423/2020/` doi: 10.5194/os-16-423-2020

Bouzinac, C., Vazquez, J., & Font, J. (1998). Complex empirical orthogonal functions analysis of in the region of the Algerian current. *Journal of Geophysical Research: Oceans*, *103*, 8059–8071. doi: 10.1029/97JC02909

Bryden, H. L., Mujahid, A., Cunningham, S. A., & Kanzow, T. (2009). Adjustment of the basin-scale circulation at 26° N to variations in Gulf Stream, deep western boundary current and Ekman transports as observed by the Rapid array. *Ocean Science*, *5*(4), 421–433. doi: 10.5194/os-5-421-2009

Carrère, L., & Lyard, F. (2003). Modeling the barotropic response of the global ocean to atmospheric wind and pressure forcing - comparisons with observations. *Geophysical Research Letters*, *30*(6). doi: 10.1029/2002GL016473

Dee, D. P., Uppala, S. M., Simmons, A. J., Berrisford, P., Poli, P., Kobayashi, S., ... Vitart, F. (2011). The ERA-Interim reanalysis: configuration and performance of the data assimilation system. *Quarterly Journal of the Royal Meteorological Society*, *137*(656), 553–597. doi: 10.1002/qj.828

Dobslaw, H., Bergmann-Wolf, I., Dill, R., Poropat, L., & Flechtner, F. (2017b). *Product Description Document for AOD1B Release 06, Rev. 6.1.* GFZ Potsdam, Potsdam, Germany. ftp://isdcftp.gfz-potsdam.de/grace/DOCUMENTS/Level-1/GRACE_AOD1B_Product_Description_Document_for_RL06.pdf. (Accessed 6 September 2021)

Dobslaw, H., Bergmann-Wolf, I., Dill, R., Poropat, L., Thomas, M., Dahle, C., ... Flechtner, F. (2017a). A new high-resolution model of non-tidal atmosphere and ocean mass variability for de-aliasing of satellite gravity observations: AOD1B RL06. *Geophysical Journal International*, *211*(1), 263–269. doi: 10.1093/gji/ggx302

Egbert, G. D., & Ray, R. D. (2001). Estimates of M_2 tidal energy dissipation from TOPEX/Poseidon altimeter data. *Journal of Geophysical Research: Oceans*, *106*(C10), 22475–22502. doi: 10.1029/2000JC000699

Einšpigel, D., & Martinec, Z. (2017). Time-domain modeling of global ocean tides generated by the full lunisolar potential. *Ocean Dynamics*, *67*, 165–189. doi: 10.1007/s10236-016-1016-1

Flechtner, F., Neumayer, K.-H., Dahle, C., Dobslaw, H., Fagiolini, E., Raimondo, J.-C., & Güntner, A. (2016). What can be expected from the GRACE-FO laser ranging interferometer for Earth science applications? *Surveys in Geophysics*, *37*, 453–470. doi: 10.1007/s10712-015-9338-y

Gebler, M. (2013). *Detection and analysis of oceanic motion using Pressure Inverted Echo Sounders (PIES).* PhD thesis, Universität Oldenburg.

Harker, A. A., Schindelegger, M., Ponte, R. M., & Salstein, D. A. (2021). Modeling ocean-induced rapid Earth rotation variations: an update. *Journal of Geodesy*, *95*(9), 110. doi: 10.1007/s00190-021-01555-z

Hirose, N., Fukumori, I., & Ponte, R. M. (2001). A non-isostatic global sea level response to barometric pressure near 5 days. *Geophysical Research Letters*, *28*(12), 2441-2444. doi: https://doi.org/10.1029/2001GL012907

King, M. J., Wheeler, M. C., & Lane, T. P. (2015). Association of convection with the 5-day Rossby-Haurwitz wave. *Journal of the Atmospheric Sciences*, *72*(9), 3309–3321. doi: 10.1175/JAS-D-14-0316.1

Kurtenbach, E., Eicker, A., Mayer-Gürr, T., Holschneider, M., Hayn, M., Fuhrmann, M., & Kusche, J. (2012). Improved daily GRACE gravity field solutions using a Kalman smoother. *Journal of Geodynamics*, *59–60*, 39–48. doi: 10.1016/j.jog.2012.02.006

Kusahara, K., & Ohshima, K. I. (2014). Kelvin waves around Antarctica. *Journal of Physical Oceanography*, *44*(11), 2909–2920. doi: 10.1175/JPO-D-14-0051.1

Kvas, A., Behzadpour, S., Ellmer, M., Klinger, B., Strasser, S., Zehentner, N., & Mayer-Gürr, T. (2019). ITSG-Grace2018: Overview and evaluation of a new GRACE-only gravity field time series. *Journal of Geophysical Research: Solid Earth*, *124*(8), 9332–9344. doi: 10.1029/2019JB017415

Landerer, F. W., Flechtner, F. M., Save, H., Webb, F. H., Bandikova, T., Bertiger, W. I., ... Yuan, D.-N. (2020). Extending the global mass change data record: GRACE Follow-On instrument and science data performance. *Geophysical Research Letters*, *47*(12), e2020GL088306. doi: https://doi.org/10.1029/2020GL088306

Luther, D. S. (1982). Evidence of a 4–6 day barotropic, planetary oscillation of the Pacific Ocean. *Journal of Physical Oceanography*, *12*(7), 644–657. doi: 10.1175/1520-0485(1982)012⟨0644:EOADBP⟩2.0.CO;2

Madden, R., & Julian, P. (1972). Further evidence of global-scale 5-day pressure waves. *Journal of Atmospheric Sciences*, *29*(8), 1464–1469. doi: 10.1175/1520-0469(1972)029⟨1464:FEOGSD⟩2.0.CO;2

Madden, R. A. (2019). How I learned to love normal-mode Rossby-Haurwitz Waves. *Bulletin of the American Meteorological Society*, *100*(3), 503–511. doi: 10.1175/BAMS-D-17-0293.1

Madzak, M., Schindelegger, M., Böhm, J., Bosch, W., & Hagedoorn, J. (2016). High-frequency Earth rotation variations deduced from altimetry-based ocean tides. *Journal of Geodesy*, *90*, 1237–1253. doi: 10.1007/s00190-016-0919-4

Mathers, E. L., & Woodworth, P. L. (2004). A study of departures from the inverse-barometer response of sea level to air-pressure forcing at a period of 5 days. *Quarterly Journal of the Royal Meteorological Society*, *130*(597), 725–738. doi: https://doi.org/10.1256/qj.03.46

Mayer-Gürr, T., Behzadpur, S., Ellmer, M., Kvas, A., Klinger, B., Strasser, S., & Zehentner, N. (2018). *ITSG-Grace2018 - Monthly, daily and static gravity field solutions from GRACE.* GFZ Data Services. doi: http://doi.org/10.5880/ICGEM.2018.003

Park, J.-H., & Watts, D. R. (2006). Near 5-day nonisostatic response of the Atlantic Ocean to atmospheric surface pressure deduced from sub-surface and bottom pressure measurements. *Geophysical Research Letters*, *33*(12), L12610. doi: https://doi.org/10.1029/2006GL026304

Ponte, R. M. (1997). Nonequilibrium response of the global ocean to the 5-day Rossby-Haurwitz wave in atmospheric surface pressure. *Journal of Physical Oceanography*, *27*(10), 2158–2168.

Ponte, R. M. (2009). Rate of work done by atmospheric pressure on the ocean general circulation and tides. *Journal of Physical Oceanography*, *39*(2), 458–464. doi: 10.1175/2008JPO4034.1

Ponte, R. M., & Hirose, N. (2004). Propagating bottom pressure signals around Antarctica at 1–2-day periods and implications for ocean modes. *Journal of Physical Oceanography*, *34*(1), 284–292. doi: 10.1175/1520-0485(2004)034⟨0284:PBPSAA⟩2.0.CO;2

Ray, R. D. (2001). Inversion of oceanic tidal currents from measured elevations. *Journal of Marine Systems*, *28*(1), 1–18. doi: 10.1016/S0924-7963(00)00081-6

Sakazaki, T., & Hamilton, K. (2020). An array of ringing global free modes discovered in tropical surface pressure data. *Journal of the Atmospheric Sciences*, *77*(7), 2519–2539. doi: https://doi.org/10.1175/JAS-D-20-0053.1

Schindelegger, M., Harker, A. A., Ponte, R. M., Dobslaw, H., & Salstein, D. A. (2021). Convergence of daily GRACE solutions and models of submonthly ocean bottom pressure variability. *Journal of Geophysical Research: Oceans*, *126*(2), e2020JC017031. doi: https://doi.org/10.1029/2020JC017031

Stepanov, V. N., & Hughes, C. W. (2004). Parameterization of ocean self-attraction and loading in numerical models of the ocean circulation. *Journal of Geophysical Research: Oceans*, *109*, C03037. doi: 10.1029/2003JC002034

Stepanov, V. N., & Hughes, C. W. (2006). Propagation of signals in basin-scale ocean bottom pressure from a barotropic model. *J. Geophys. Res. Oceans*, *111*, C12002. doi: 10.1029/2005JC003450

Tapley, B. D., Watkins, M. M., Flechtner, F., Reigber, C., Bettadpur, S., Rodell, M., … Velicogna, I. (2019). Contributions of GRACE to understanding climate change. *Nature Climate Change*, *9*(5), 358–369. doi: 10.1038/s41558-019-0456-2

Thomson, R. E., & Fine, I. V. (2021). Revisiting the ocean's non-isostatic response to 5-day atmospheric loading: New results based on global bottom pressure records and numerical modeling. *Journal of Physical Oceanography*, *51*, 2845–2859. doi: 10.1175/JPO-D-21-0025.1

van Dam, T., Collilieux, X., Wuite, J., Altamimi, Z., & Ray, J. (2012). Nontidal ocean loading: amplitudes and potential effects in GPS height time series. *Journal of Geodesy*, *86*(11), 1043–1057. Retrieved from `https://doi.org/10.1007/s00190-012-0564-5` doi: 10.1007/s00190-012-0564-5

Woodworth, P. L., Windle, S. A., & Vassie, J. M. (1995). Departures from the local inverse barometer model at periods of 5 days in the central South Atlantic. *Journal of Geophysical Research: Oceans*, *100*(C9), 18281–18290. doi: https://doi.org/10.1029/

95JC01741
Zhao, R., Zhu, X.-H., & Park, J.-H. (2017). Near 5-day nonisostatic response to atmospheric surface pressure and coastal-trapped waves observed in the northern South China Sea. *Journal of Physical Oceanography*, *47*(9), 2291–2303. doi: 10.1175/JPO-D-17-0013.1

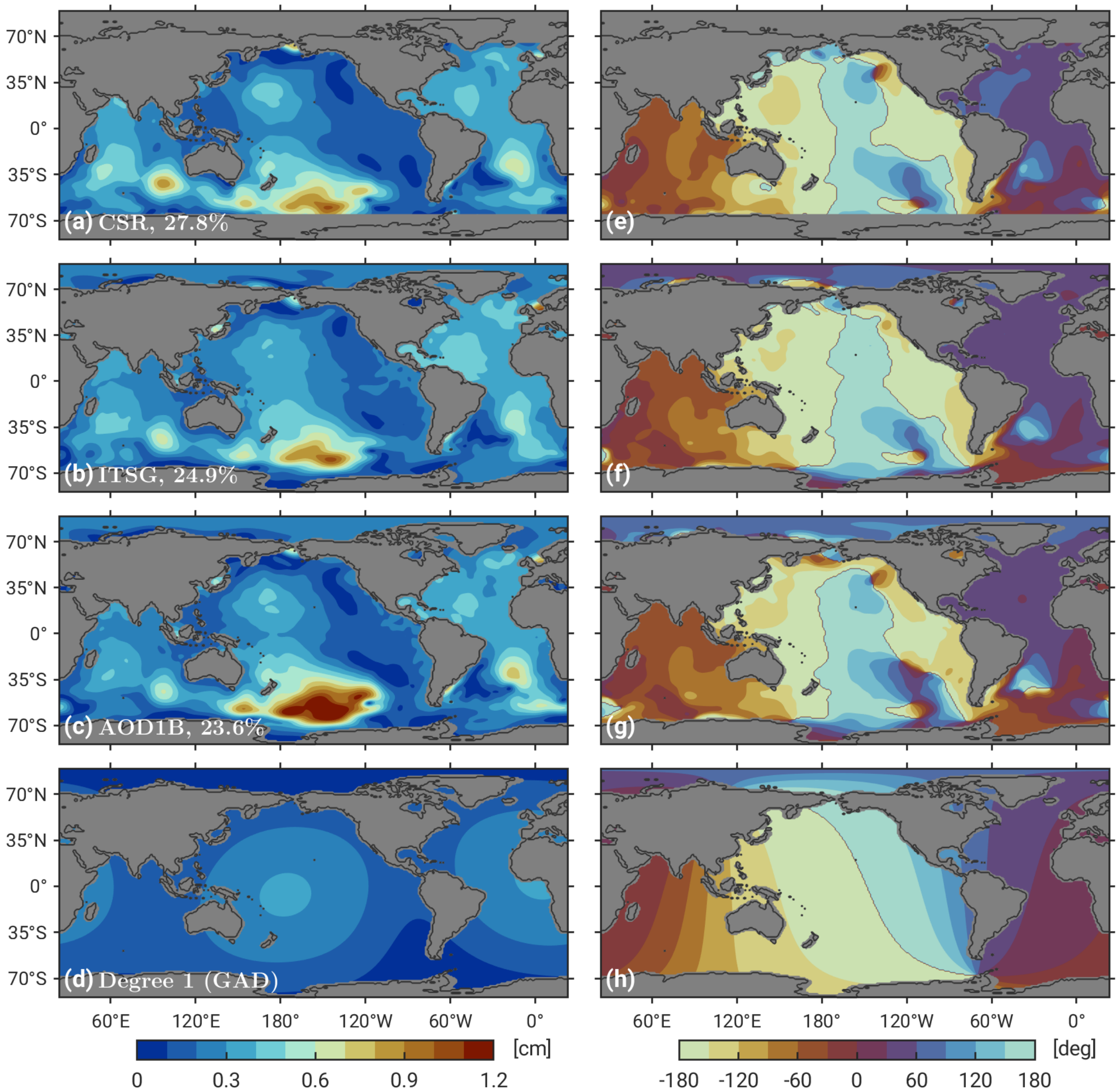

Figure 1. Spatial amplitudes in cm (left panels) and phases in degrees (right panels) of the leading mode in a Complex Empirical Orthogonal Function (CEOF) decomposition of bottom pressure anomalies at ∼5-day period, for (a,e) CSR, (b,f) ITSG, (c,g) AOD1B, and (d,h) GAD degree-1 terms from AOD1B RL06. Amplitudes are calculated as the standard deviation of the mode's time series synthesized from the CEOF results. Phase propagation is in the direction of increasing phase values. Phase contours are drawn such that the associated temporal mode has 0° phase at the initial analysis time (1 January 2007, 12 UTC). Percentage of total variance explained by the CEOF is also given.

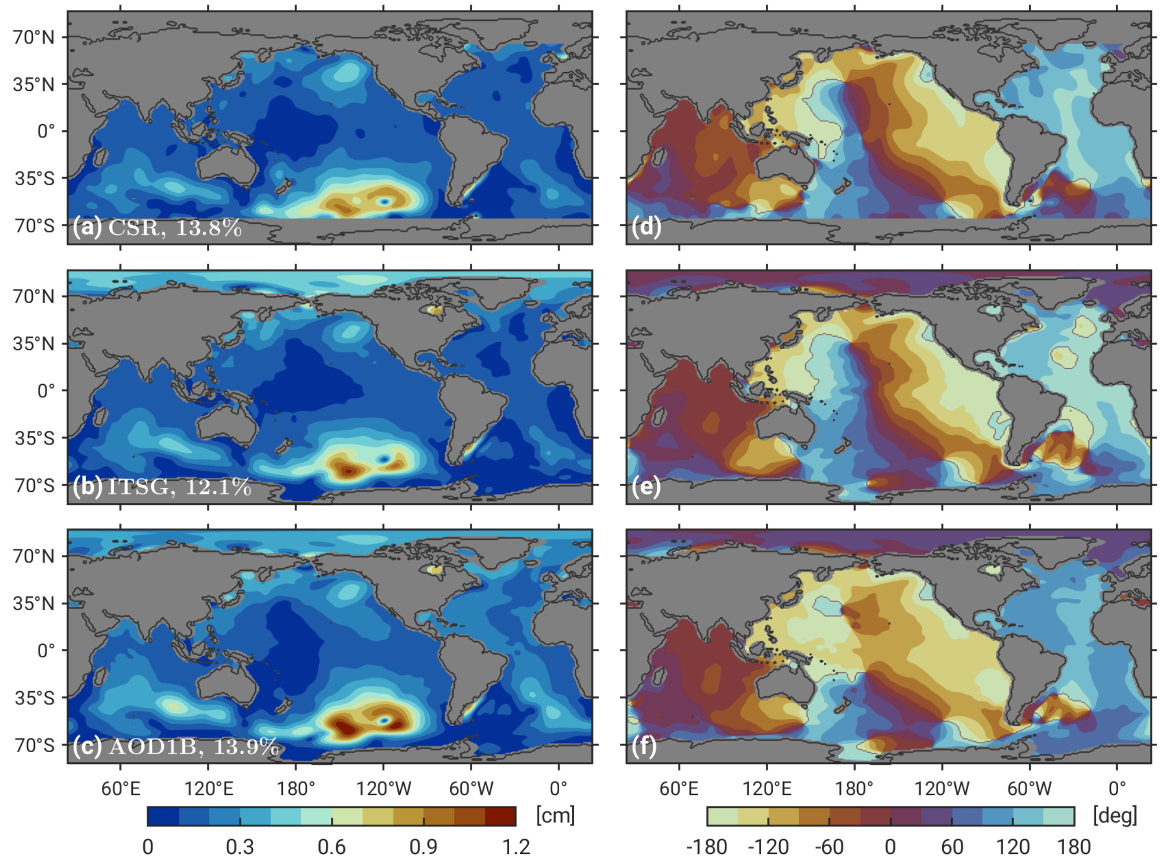

Figure 2. As in Figure 1 but for CEOF2 and without separate panels for degree $n = 1$ signals.

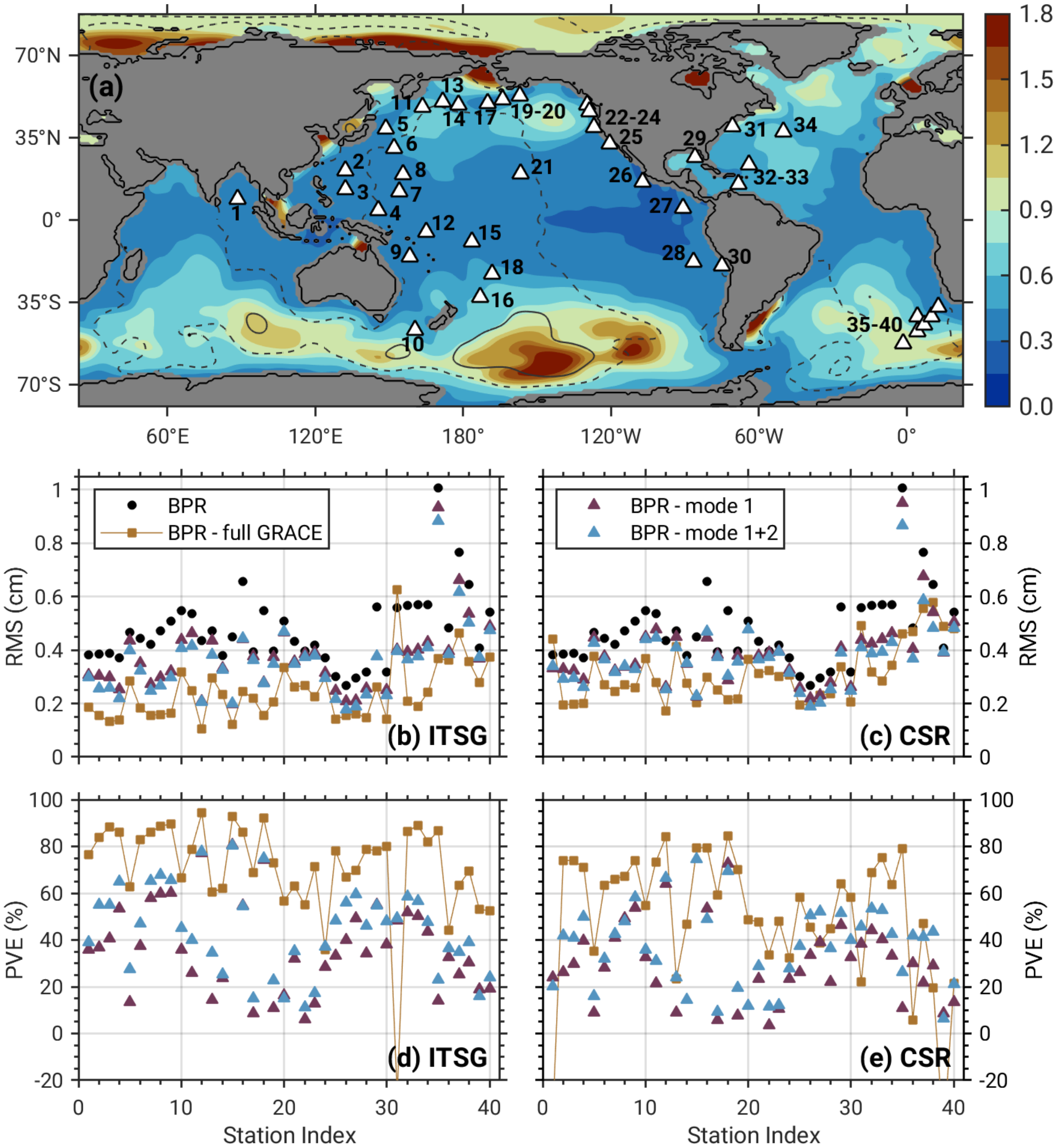

Figure 3. (a) Standard deviation of p_b variations (cm) in the 5-day band, taken from ITSG. Dashed and solid lines are the 2.5 and 6 mm contours of the ITSG CEOF1 standard deviation. Panels (b) and (c) show RMS differences from the comparison of 5-day ITSG and CSR swath mass anomalies with observations from 40 BPRs, plotted in panel (a) and labelled by increasing longitude. Black circles are RMS values of the filtered BPR signals, while RMS differences are displayed for the filtered GRACE series (orange squares), CEOF1 (purple triangles), and the sum of CEOF1 and CEOF2 (blue triangles). Panels (d) and (e) show the corresponding PVE values. Note that degree $n = 1$ contributions are contained in all comparisons.

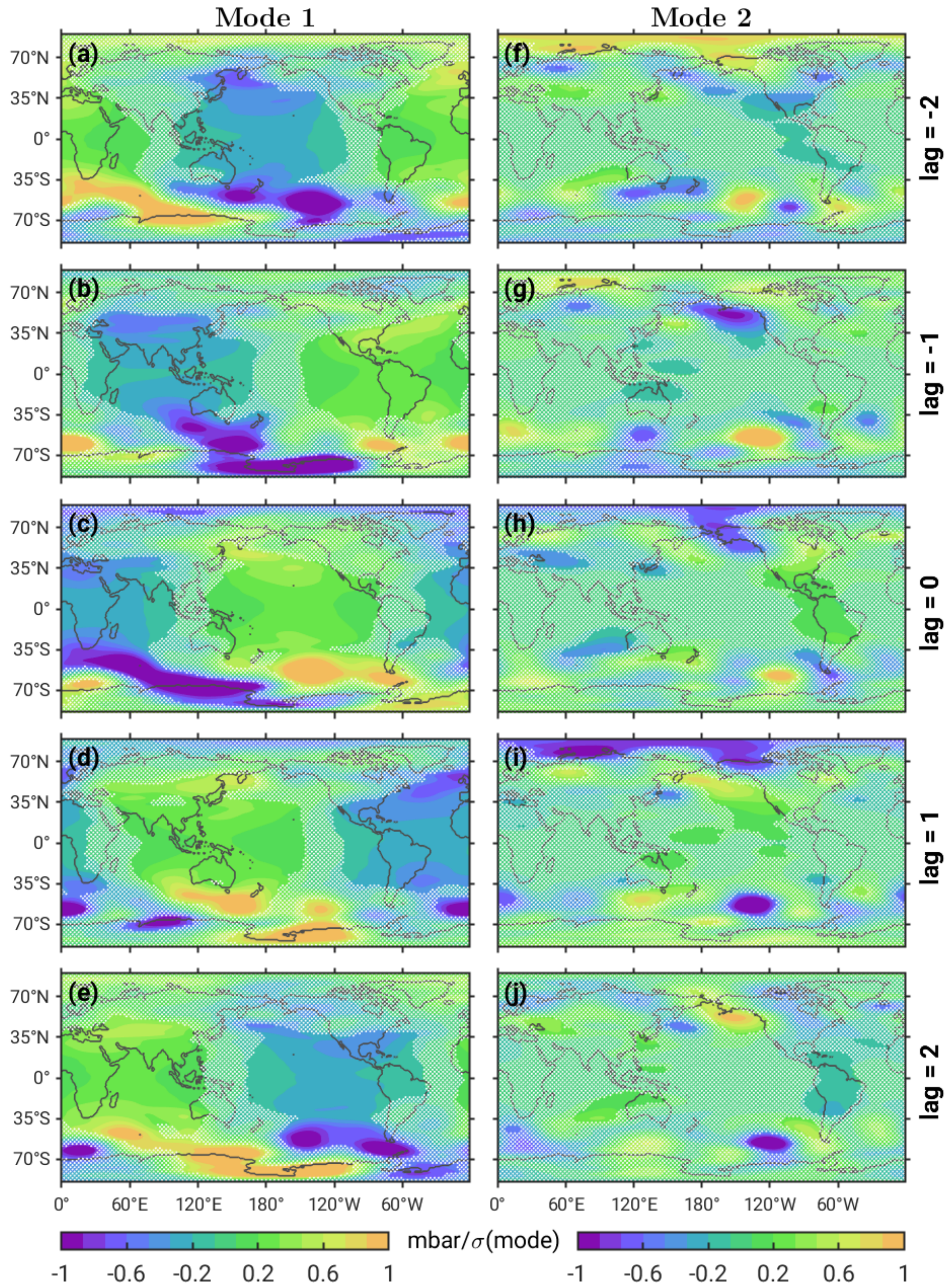

Figure 4. Lagged-regression coefficients between time-dependent modifications of (a)–(e) CEOF1 and (f)–(j) CEOF2 from ITSG and ERA-Interim sea level pressure anomalies in the 5-day band. Lags are reckoned in days and regression units are mbar per standard deviation of the respective temporal mode. Only the real part of the mode (with phase set to 0° at initial analysis time) was considered in the regression. White stipples indicate areas where the lagged-correlation coefficient is below the 95% confidence level with a two-tailed *t* test (0.21 for both modes, after accounting for serial correlation).

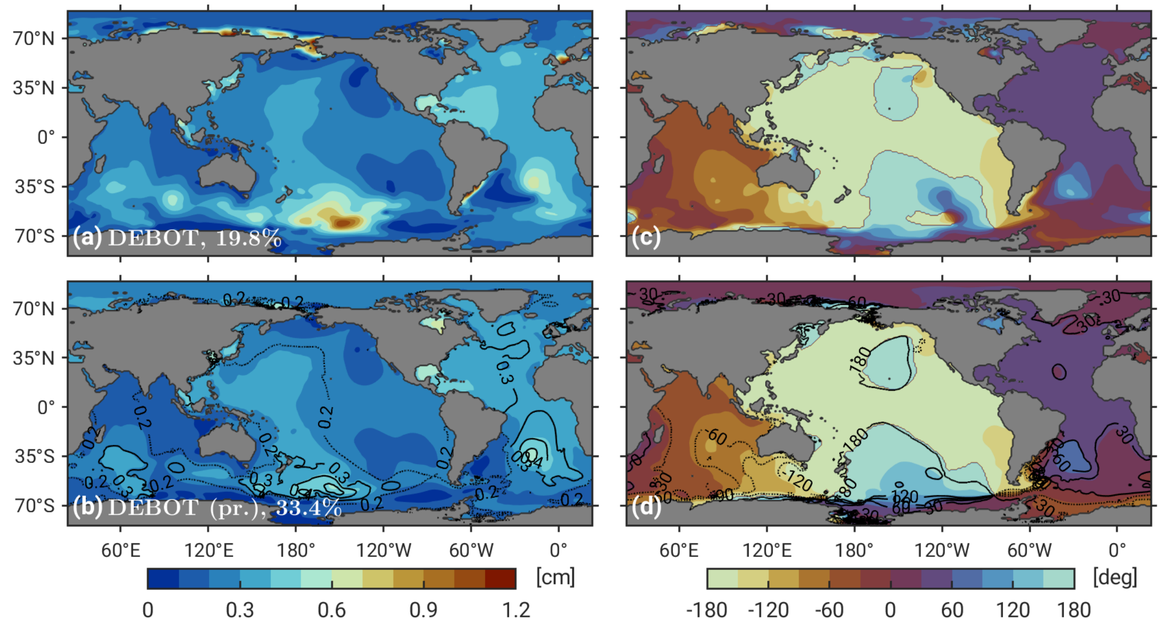

Figure 5. CEOF1 spatial amplitudes (left panels, as standard deviations in cm) and phases (right panels, deg) in ∼5-day p_b anomalies from simulations with DEBOT. Upper row shows results from a 3-year run with pressure and wind forcing, while charts in the bottom row are for pressure forcing (P_a) only. Superimposed on (b) and (d) as contour lines are standard deviations and phases from a simulation with harmonic 5-day P_a forcing, as deduced from the regression results for mode 1 (see Figure 4). Phase convention is as in Figure 1. Percentage of total variance explained by CEOF1 is included in the labels of (a) and (b).

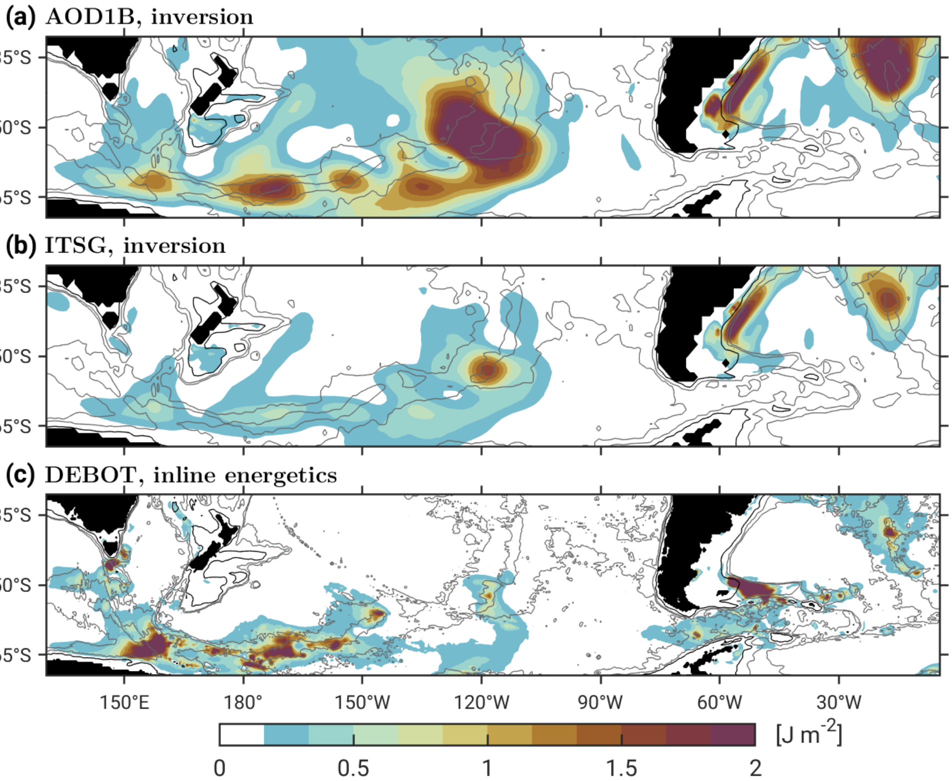

Figure 6. Local kinetic energy (J m^{-2}) of the oceanic 5-day signal, computed over an extended sector of the Southern Ocean from (a,b) CEOF1 p_b maps of AOD1B and ITSG (Figure 1) and (c) dynamical fields (p_b, $\mathbf{u}$) in a DEBOT simulation with 5-day P_a forcing. The flow fields underlying panels (a) and (b) were deduced using a least-squares inversion approach, see the main text. Thin lines are isobaths at 1000, 3000, and 4000 m, with the 1000-m contour shown in black. Note the difference in grid spacing between inversion and DEBOT results (1° vs. ⅓°).